



Hugoniot Data and Equation of State Parameters for an Ultra-High Performance Concrete

C. Sauer¹ · F. Bagusat¹ · M.-L. Ruiz-Ripoll² · C. Roller² · M. Sauer¹ · A. Heine¹ · W. Riedel¹

Received: 17 February 2021 / Accepted: 17 June 2021 / Published online: 20 July 2021
© The Author(s) 2021

Abstract

This work aims at the characterization of a modern concrete material. For this purpose, we perform two experimental series of inverse planar plate impact (PPI) tests with the ultra-high performance concrete B4Q, using two different witness plate materials. Hugoniot data in the range of particle velocities from 180 to 840 m/s and stresses from 1.1 to 7.5 GPa is derived from both series. Within the experimental accuracy, they can be seen as one consistent data set. Moreover, we conduct corresponding numerical simulations and find a reasonably good agreement between simulated and experimentally obtained curves. From the simulated curves, we derive numerical Hugoniot results that serve as a homogenized, mean shock response of B4Q and add further consistency to the data set. Additionally, the comparison of simulated and experimentally determined results allows us to identify experimental outliers. Furthermore, we perform a parameter study which shows that a significant influence of the applied pressure dependent strength model on the derived equation of state (EOS) parameters is unlikely. In order to compare the current results to our own partially reevaluated previous work and selected recent results from literature, we use simulations to numerically extrapolate the Hugoniot results. Considering their inhomogeneous nature, a consistent picture emerges for the shock response of the discussed concrete and high-strength mortar materials. Hugoniot results from this and earlier work are presented for further comparisons. In addition, a full parameter set for B4Q, including validated EOS parameters, is provided for the application in simulations of impact and blast scenarios.

Keywords Ultra-high performance concrete · Hugoniot data · Planar plate impact test · p - α equation of state · RHT model

Introduction

Concrete is widely predominant in modern architecture and hence a very relevant material regarding its response to any kind of mechanical loading. Recently, ultra-high performance concrete (UHPC) has become more relevant for applications, for example in bridge engineering [1], resilient core structures of high rise buildings [2], and protective structures for critical infrastructure [3]. The unconfined compressive strength of such UHPC materials ranges from approximately

100 to 200 MPa [1], which is somewhere between three and six times the strength of conventional concrete.

In addition to knowing the static and low rate (earth quakes etc.) response of concrete building structures, there is also the desire to model their high-rate loading behavior in order to predict their reaction to blast and impact scenarios [4–12]. At the increasing pressures produced in such scenarios, the material response progressively becomes less dependent on strength, and a proper treatment of the equation of state (EOS) is necessary to accurately predict dynamic material behavior [13, 14]. Reaching very high pressures and entering the regime of hydrodynamic behavior and shock wave propagation, the EOS can even become dominant. Examples for such EOS dominated material response are contact detonation [6, 15, 16] and hypervelocity impact of projectiles [9, 11, 17, 18] and metal jets [12, 19].

The planar plate impact (PPI) test is an established technique to investigate EOS properties under shock loading [13, 20, 21] that has been applied to a variety of different materials, such as metals, composites, concretes and geomaterials

✉ C. Sauer
christoph.sauer@emi.fraunhofer.de

¹ Fraunhofer Institute for High-Speed Dynamics, Ernst-Mach-Institut, EMI, Ernst-Zermelo-Str. 4, 79104 Freiburg, Germany

² Fraunhofer Institute for High-Speed Dynamics, Ernst-Mach-Institut, EMI, Am Klingelberg 1, 79588 Efringen-Kirchen, Germany

[15, 22–36]. Hugoniot data derived from these experiments is available for different types of concrete [15, 22–25, 27, 29] and mortar materials [27, 31, 33]. In this work, mortar is referred to as a mix of cement and water (and other additives) with only fine aggregates (like sand or other fine powder) while concrete is used for mortar binding larger aggregates (gravel and other rock) and steel fibers. The Hugoniot data of different mortar and concrete materials has been compared in [27] and more recently in [33]. The latter also includes an extensive review of published and partly so far not publicly available Hugoniot data [33].

In the available literature, various findings with respect to the comparison of the Hugoniot data of different concretes and mortars are presented. Whenever agreement between different sets of Hugoniot data is reported, it should be considered that there can be significant scattering in each of the regarded data sets and hence, the found agreement is within the observed experimental uncertainties. This issue is somewhat expected for a heterogenous material like concrete. Hall et al. [24] find no strong dependence on aggregate size for the Hugoniot data of different concretes. Moreover, experimental investigations of conventional and high-strength mortar by Riedel et al. [27] reveal a significantly different shock response for the two mortars (without replacing larger aggregate by fine grain material) and based on this data also predict differences for conventional and high-strength concrete with meso-mechanical simulations. Additionally, Reinhart [29] discusses effects of the admixture of steel fibers, aggregates and both, while no significant influence of unconfined compressive strength on the Hugoniot data is mentioned. Furthermore, Neel [33] argues that material specific behavior is only present in the pore compaction regime for shock velocity vs. particle velocity data. In this region a dispersive compression wave is produced, which is influenced by material specific characteristics as initial density, a complex interplay of different competing processes, and the compacted density. Moreover, Neel [33] states that at higher Hugoniot stress, most concretes and mortars exhibit the same shock response, regardless of strength or the admixture of aggregates and steel fibers. Consequently, an interesting discussion is ongoing in the literature on the shock properties of concrete and mortar.

With this work, we want to contribute to this discussion by extending the available Hugoniot data with a consistent and highly reliable data set for a UHPC named B4Q. Furthermore, it is our objective to enable numerical applications of high-rate loading by providing validated EOS parameters for this material. The B4Q recipe has been developed at the University of Kassel [37]. It contains aggregates with a maximum grain size of 8.0 mm as well as steel fibers. The material investigated here exhibits an unconfined, compressive cylinder strength of $f_c = 140$ MPa. It is thus in the medium strength range of UHPC materials.

This material has previously been investigated with respect to impact [2, 38] at velocities below 400 m/s.

In order to derive a highly reliable Hugoniot data set for B4Q, two different experimental configurations of inverse PPI tests with varying backing and witness plate materials are implemented. Since shock and strength behavior of these plate materials need to be known to derive the Hugoniot data of the specimen material in the applied sandwich configuration, any inaccuracy in these material properties will obscure the obtained Hugoniot data of B4Q. However, comparing the results of these two experimental series to one another, a significant influence of possible inaccuracies stemming from the involvement of the plate materials in the derivation of the Hugoniot data should become visible. Additionally, we successfully reproduce the experimentally determined free surface velocity time curves with numerical simulations. This allows us to compare the experimental with the corresponding numerical Hugoniot results. The latter originate from a perfectly homogenous B4Q material model using EOS parameters that are validated with the Hugoniot plateau and additional features from the experimental curves. Altogether, the consistent picture of results from two experimental series and corresponding numerical simulations allows us to present a highly trustworthy Hugoniot data set that can be included in the ongoing discussion about shock properties of concrete and mortar. Moreover, the reproduction of the data with numerical simulations results in validated EOS parameters for B4Q that are available for numerical applications of high-rate loading scenarios.

In the following, we start with a brief presentation of the experimental setup of the conducted PPI experiments before we present the free surface velocity time curves of the two conducted experimental series. The presented curves are discussed and the derivation of Hugoniot data from these curves is explained. After that, we compare the resulting shock velocity vs. particle velocity and stress vs. strain values of both series and relate data points deviating from the observed trend lines to features in the previously shown free surface velocity time curves. Then, we introduce the setup of the numerical simulations and explain the determination of the employed simulation parameters. The following comparison of experimentally and numerically produced velocity time curves and the Hugoniot data derived from these curves allows us to identify the previously discussed data points as experimental outliers. After that, a parametric study is given that enables us to discuss the influence of strength parameters on free surface velocity time curves. Then, we apply the derived parameter set for B4Q to a numerical extrapolation of the derived shock information and compare all results of our present work with earlier work and selected literature data. Finally, a conclusion of our experimental and numerical work on the shock response of B4Q is presented.

Planar Plate Impact Experiments

In the following, the setup of two experimental series, mainly differing by the employed plate materials C45 steel and aluminum 7075 T6, are presented. The former has been used in previous own studies [27, 30, 32, 34, 35] while the latter is a rather novel material for our PPI experiments. One reason for the choice of aluminum is that its shock impedance is sufficiently high to be used in inverse PPI experiments with concrete: the density of Al 7075 T6 is slightly higher (> 10%), while the wave velocity clearly exceeds (> 50%) that of concrete. Moreover, aluminum will show no phase transition (expected at 220 GPa [39]) under the loading conditions realized by the impact velocities used here, whereas steel exhibits a phase transition at about 13 GPa [40]. The differing shock and strength properties of both witness plate materials allow us to reveal possible inaccuracies stemming from those

materials in the derived Hugoniot data of the UHPC specimen. For that, the Hugoniot data of both conducted series is directly compared to one another after the free surface velocity time curves, from which this data is derived, are shown and discussed. In addition, data points that deviate from the trend in the combined Hugoniot data are discussed in relation to features in these curves.

Experimental Setup

The two series of PPI experiments used for characterizing Hugoniot properties of B4Q have been conducted at two different single stage acceleration facilities located at EMI Freiburg. Figure 1 illustrates the experimental setup of both series schematically. In principle, the experiments in this work are analogous to former investigations on concrete [27], sandstone [32], adobe [34], and masonry brick material [35]. In all cases, the specimen was bonded to a backing plate with a two component epoxy, then the

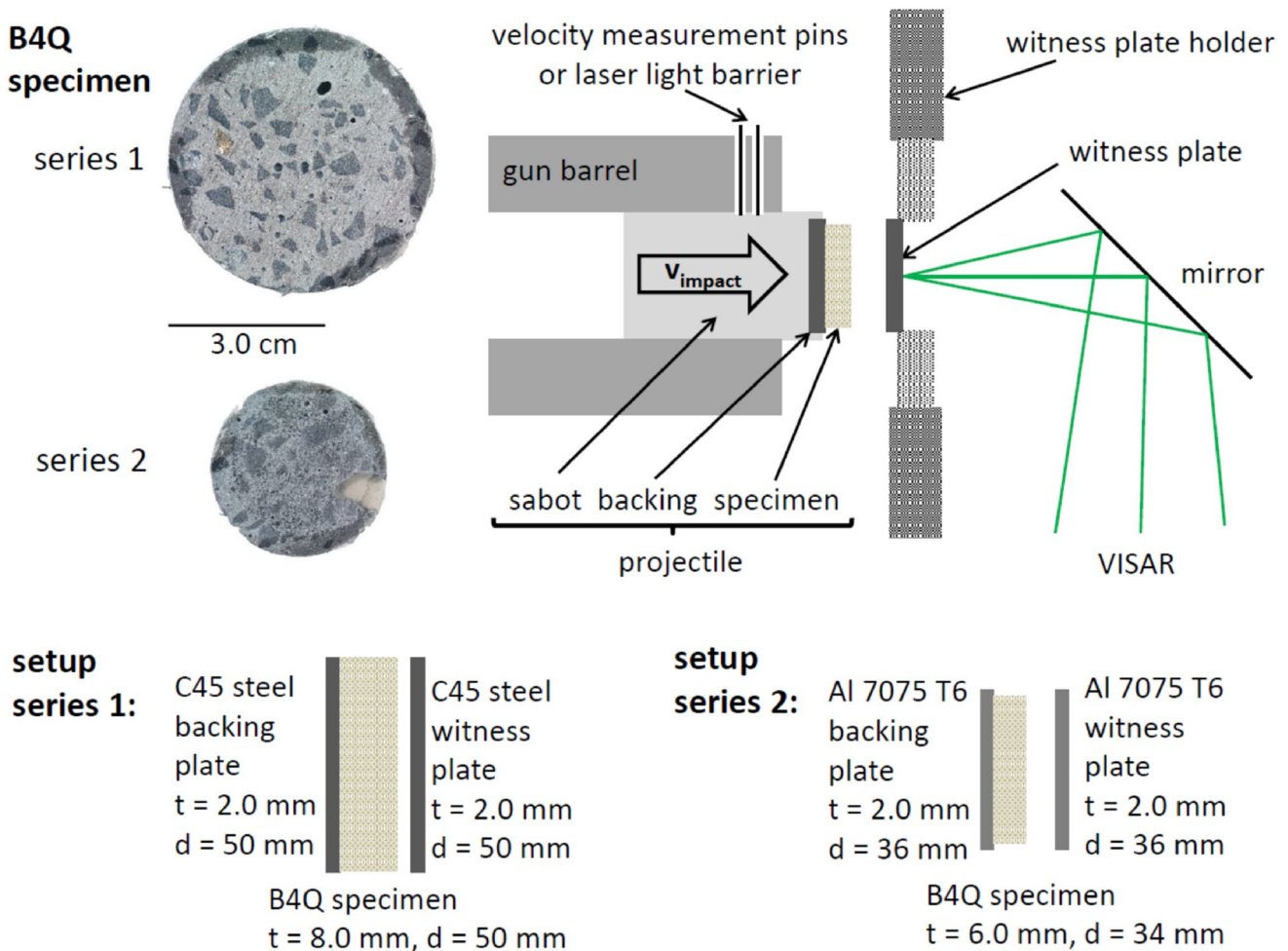


Fig. 1 Schematic picture of the experimental setup of the inverse planar plate experiments (upper right) performed with the B4Q specimen (upper left). The bottom displays the two setups for both series with different plate materials, thicknesses t and diameters d

specimen-backing plate combination was attached to a solid polycarbonate sabot, which was accelerated. One series of experiments (series 1) was executed with C45 steel for the backing and witness plate (each plate with a diameter of $d=50$ mm and a thickness of $t=2.0$ mm). These samples were accelerated in a gun barrel with an inner diameter of 70 mm. The other series (series 2) was performed with Al 7075 T6 for the backing and witness plate (diameter of $d=36$ mm, thickness of $t=2.0$ mm) and samples were accelerated in a gun barrel with a bore diameter of 42 mm. The thickness t of the specimen ($t=8.0$ or 6.0 mm) was adapted to maintain a similar sample diameter to thickness ratio. Impact conditions of the inverse experiments enabled a high planarity (~ 1 mrad) as known from direct PPI [26].

The single point measurement laser spot of the VISAR interferometer [41–43] with a diameter of about 0.5 mm is positioned in the center of the rear surface of the witness plate. By measuring the surface velocity of the metallic witness plate in this indirect PPI setup, the poor reflectance of the concrete specimen is circumvented. Simultaneously, effects of inhomogeneities of the specimen (aggregates and voids) are somewhat averaged out by the wave propagation through the witness plate prior to the surface velocity measurement. However, since in the B4Q specimens (top left in Fig. 1), the size of aggregates and voids can be larger than the measurement spot, some influence of inhomogeneity is still expected in the data. Especially considering the maximum grain size of the aggregates (8.0 mm) in B4Q with respect to the sample thicknesses ($t=8.0$ or 6.0 mm), a single measurement might be strongly dominated by the contribution of a large aggregate grain. This extreme case, however, is quite unlikely and can be identified via an overview of the entire data set and its comparison to numerical

simulations. Since there is only a content of 1.0 volume percent of steel fibers in B4Q, a significant contribution of this component to the data is not expected.

The applied VISAR interferometer enables a time resolution of better than 2 ns. The free surface velocity is recorded with a typical accuracy of ± 0.5 – 1.0% in case of the setup of series 1 and ± 1 – 2% in case of the setup of series 2, depending on the number of recorded interference fringes [44]. Al 7075 T6 as witness plate material generated steeper signal increases of the free surface velocity, so that a larger VISAR constant needed to be applied, which reduced the number of fringes. All experiments were conducted with specimens conditioned at room temperature (21 ± 2 °C). Moreover, the impact velocity is measured with an accuracy of at least $\pm 3\%$ for series 1, where trigger pins are applied, and with an accuracy of $\pm 1\%$ for series 2, where a laser light barrier is used. Primary signals of the VISAR were recorded by an oscilloscope with a sample rate of 5 GHz.

Free Surface Velocity Time Curves

Upon impact of the projectile on the witness plate (see Fig. 1) a common Hugoniot stress is created at the interface between specimen and witness plate. From this interface, shock waves travel through both the witness plate and the specimen. When this initial shock wave reaches the rear surface of the witness plate, an increase of the free surface velocity is measured with the VISAR. The corresponding plateau of the surface velocity time curve is called the first Hugoniot plateau (see Fig. 2) and its height carries information of the shock loading of the specimen and the witness plate material. With the known shock properties of the latter, the Hugoniot data of B4Q can be derived.

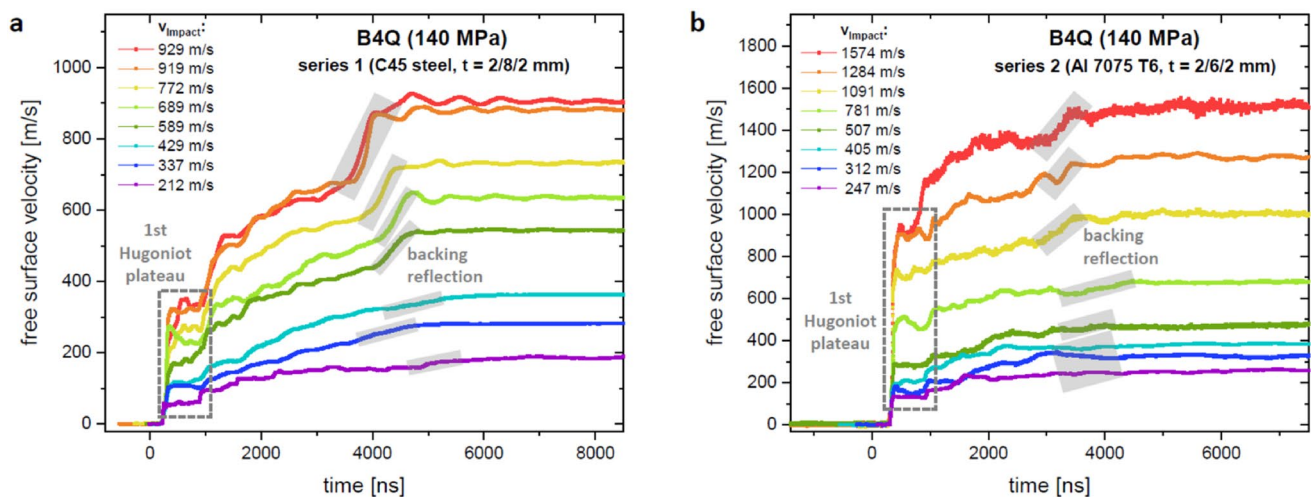


Fig. 2 Free surface velocity time curves from both conducted series of planar plate experiments with the ultra-high performance concrete B4Q. Details on the different setups of series 1 (a) and series 2 (b) are illustrated in Fig. 1 (Color figure online)

After the initial shock wave is reflected at the free surface, it travels back into the witness plate as a release wave and is then again reflected (and transmitted) at the interface to the B4Q specimen. The compression waves produced by a multiple of such reflections subsequently reach the free surface and lead to several higher velocity plateaus that carry information of release states in B4Q. Then, after the formation of several of these release plateaus, the so-called backing reflection arrives at the free surface and produces a further major velocity increase (see Fig. 2) that accelerates the free surface to the final velocity. The backing reflection is a consequence of the initial shock wave that was reflected at the specimen-backing plate interface and travelled all the way back to the VISAR measurement spot. The arrival time of this signal thus carries information of the average wave propagation speed in the sample as well as its compaction behavior under shock and re-shock. A depiction and more detailed description of wave propagation in the inverse PPI setup and its relation to the resulting free surface velocity time curve is given in [34]. Stress–particle velocity plots for different plate dimensions of the inverse PPI setup are introduced in [27].

In Fig. 2, the free surface velocity time curves of both experimental series are presented. In each series, eight successful experiments with different impact velocities have been conducted. For all of these curves, the expected features for an inverse PPI test with a porous material are present in the data [27, 32, 34, 35]. Explicitly, each curve shows a first Hugoniot plateau, several release plateaus, and a backing reflection. The velocity increase and slope of the latter feature decrease towards lower impact velocities; however, this feature is less pronounced in the curves of series 2. Moreover, the final velocities reached in all curves of both series follow a trend that is expected from the corresponding impact velocities. Similarly, the heights of the Hugoniot plateaus and the arrival times of the backing reflections are consistent with each other, except for one curve in each series. For series 1, when compared to the other curves, the one with an impact velocity of 337 m/s (dark blue in Fig. 2a) exhibits an Hugoniot plateau that is higher and a backing reflection that arrives earlier than expected. For series 2, in Fig. 2b, it is the curve with an impact velocity of 1574 m/s (red), for which the height of the Hugoniot plateau appears too low and the arrival of the backing reflection too late in comparison to the other curves. These two curves and the Hugoniot data derived from them will be given special attention in the following discussions. At first glance, the rest of the data in Fig. 2 appears to exhibit a comparatively low scatter for an inhomogeneous material like B4Q. In none of these curves, a characteristic drop in velocity associated with possible edge release waves can be observed before the final velocities are reached.

Hugoniot Data

The Hugoniot data of B4Q is calculated from the height of the first Hugoniot plateau u_{fs_2} , the impact velocity v_{imp} of the PPI experiment, and a set of constants for B4Q and the applied witness plate material (subscript WP). The formulas for the calculation of the Hugoniot stress σ_H and strain ϵ , the particle velocity u_p , and the shock velocity U_s are [30, 32, 34]:

$$u_{p,WP} \approx \frac{1}{2}u_{fs_2} \quad (1)$$

$$U_{s,WP} = c_{B,WP} + S_{WP}u_{p,WP} \quad (2)$$

$$\text{For } u_{fs_2} \leq u_{HEL,WP} : \quad \sigma_H = \frac{1}{2}\rho_{WP}c_{p,WP}u_{fs_2}^2 \quad (3)$$

$$\begin{aligned} \text{For } u_{fs_2} > u_{HEL,WP} : \quad \sigma_H &= \frac{1}{2}\rho_{WP}c_{p,WP}u_{HEL,WP}^2 \\ &+ \frac{1}{2}\rho_{WP}U_{s,WP}(u_{fs_2} - u_{HEL,WP}) \end{aligned} \quad (4)$$

$$u_{p,B4Q} = v_{imp} - u_{p,WP} = v_{imp} - \frac{1}{2}u_{fs_2} \quad (5)$$

$$U_{s,B4Q} = \frac{\sigma_H}{\rho_{B4Q}u_{p,B4Q}} \quad (6)$$

$$\epsilon_{B4Q} = \frac{u_{p,B4Q}}{U_{s,B4Q}} \quad (7)$$

Further details on these formulas are given in [30, 32, 34]. For C45 steel, the initial density $\rho_{steel} = 7.8 \text{ g/cm}^3$, shock parameters of slope $S_{steel} = 1.332$, and bulk sound velocity $c_{B,steel} = 4483 \text{ m/s}$ are employed together with longitudinal wave velocities of $c_{p,steel} = 5830 \text{ m/s}$ for $u_{fs_2} \leq u_{HEL,steel}$ and $c_{p,steel} = 6000 \text{ m/s}$ for $u_{fs_2} > u_{HEL,steel}$ [26, 30, 32, 34, 40]. The Hugoniot elastic limit of $u_{HEL,steel} = 36 \text{ m/s}$ of the current C45 steel lot corresponds to the elastic precursor signals visible in the free surface velocity time curves. In earlier works [27, 30, 32, 34, 35] a hardened C45 steel with a higher yield strength and hence a larger value for $u_{HEL,steel}$ has been used. For Al 7075 T6, the corresponding constants are $\rho_{Al} = 2.804 \text{ g/cm}^3$, $S_{Al} = 1.36$, $c_{B,Al} = 5200 \text{ m/s}$, $u_{HEL,Al} = 160 \text{ m/s}$, and $c_{p,Al} = 6300 \text{ m/s}$ for all u_{fs_2} values [45]. Additionally, an averaged initial density of $\rho_{B4Q} = 2.39 \text{ g/cm}^3$ is used for the B4Q specimen. With these constants and the given Eqs. (1)–(7), the Hugoniot data for both PPI series is calculated and given in Table 1. Due to the realized one-dimensional strain state, this strain is equal to the

Table 1 Experimentally determined impact velocities v_{imp} and Hugoniot plateau heights $u_{fs,2}$ together with derived shock material data (Hugoniot stress σ_H , strain ϵ , particle velocity u_p , and shock velocity U_s) of the UHPC B4Q for series 1 (C45 steel plates, thicknesses 2.0/8.0/2.0 mm) and series 2 (Al 7075 T6 plates, thicknesses 2.0/6.0/2.0 mm)

Experiment number	v_{imp} (m/s)	$u_{fs,2}$ (m/s)	σ_H (MPa)	ϵ_{B4Q} (%)	$u_{p,B4Q}$ (m/s)	$U_{s,B4Q}$ (m/s)
Series 1						
E4179	212 ± 6	57.9 ± 2.6	1229 ± 47	6.5 ± 0.9	183 ± 8	2808 ± 234
E4178	337 ± 10	107.0 ± 0.8	2103 ± 15	9.1 ± 0.8	284 ± 11	3104 ± 143
E4180	429 ± 13	117.4 ± 3.8	2290 ± 69	14.3 ± 1.7	370 ± 15	2588 ± 188
E4172	589 ± 18	177.1 ± 9.4	3374 ± 172	17.7 ± 2.7	500 ± 22	2821 ± 283
E4176	689 ± 21	229.1 ± 4.0	4333 ± 75	18.2 ± 1.8	574 ± 23	3156 ± 187
E4177	772 ± 23	266.3 ± 6.4	5028 ± 121	19.4 ± 2.2	639 ± 27	3293 ± 224
E4175	919 ± 28	317.8 ± 4.5	6002 ± 85	23.0 ± 2.2	760 ± 30	3304 ± 184
E4174	929 ± 28	338.7 ± 9.0	6401 ± 173	21.5 ± 2.5	760 ± 32	3526 ± 256
Series 2						
ma-1199	247 ± 3	132.1 ± 1.2	1167 ± 11	6.7 ± 0.4	181 ± 4	2698 ± 80
ma-1190	312 ± 3	155.0 ± 7.8	1369 ± 69	9.6 ± 1.1	235 ± 7	2443 ± 200
ma-1183	405 ± 4	205.3 ± 5.2	1752 ± 39	12.5 ± 0.9	302 ± 7	2425 ± 110
ma-1200	507 ± 5	278.4 ± 3.7	2308 ± 29	14.0 ± 0.7	368 ± 7	2625 ± 83
ma-1202	781 ± 8	471.5 ± 18.4	3824 ± 148	18.6 ± 2.0	545 ± 17	2935 ± 213
ma-1201	1091 ± 11	701.8 ± 7.3	5726 ± 62	22.9 ± 1.2	740 ± 15	3237 ± 101
ma-1186	1284 ± 13	896.5 ± 15.0	7412 ± 133	22.5 ± 1.6	836 ± 21	3711 ± 162
ma-1203	1574 ± 16	919.4 ± 25.9	7615 ± 231	39.0 ± 3.3	1114 ± 29	2859 ± 165

compression η of B4Q ($\eta = u_p/U_s = \epsilon$) and the compressed density of B4Q $\rho_{B4Q,comp} = \rho_{B4Q}/(1 - \epsilon_{B4Q})$ can be computed with the given strain values. The error bar values of the calculated quantities are determined by a maximum error assumption using Eqs. (1)–(7). For that, we only consider the uncertainties in measuring the impact velocity and determining the height of the Hugoniot plateau $u_{fs,2}$. The latter uncertainty is given by the standard deviation of the $u_{fs,2}$ values within the time interval of the analysis. It is hence a measure for how much the Hugoniot plateau deviates from a perfectly constant plateau, which is also correlated to the magnitude of inhomogeneity present in the specimen area below the measurement spot [29].

The values given in Table 1 are presented in Fig. 3 as shock velocity over particle velocity (a) and Hugoniot stress over strain (b). In both plots, the values from series 1 (C45 steel plates) are presented as black squares while the ones from series 2 (Al 7075 T6 plates) are shown as grey diamonds.

In both panels of Fig. 3, one data point of each series does not lie within the trend of the rest of the data and is marked with the experiment number. For series 1, this data point originates from experiment E4178 ($v_{imp} = 337$ m/s) and for series 2, it is experiment ma-1203 ($v_{imp} = 1574$ m/s). These are the experiments that lead to the two free surface velocity time curves (dark blue in Fig. 2a and red in Fig. 2b) which have been previously discussed with respect to a deviation from the otherwise observed trends in the data. Consequently, this finding in Fig. 2 becomes even clearer in the plots of the Hugoniot data in Fig. 3, which entirely originate from the heights of the Hugoniot plateaus. Here, the two

marked data points are identified as experimental outliers. An additional discussion of these data points will be given in the comparison of the data with the simulation results in the following section.

Besides these two outliers, the comparison of the Hugoniot data of both experimental series in Fig. 3 shows that the values derived from the PPI experiments with the two different setups (see Fig. 1) do not differ significantly. Hence, within the experimental accuracy that is illustrated by the depicted error bars, the Hugoniot data from both series can be seen as one data set. The fact that this consistent Hugoniot data set originates from two different experimental series with different witness plate materials makes it highly trustworthy, since any significant inaccuracy stemming from one of the plate materials should become obvious in the direct comparison of Fig. 3.

Simulation of Planar Plate Impact Tests

In this section, the results of simulations of the PPI tests are compared with the data presented in the previous section. For that, we first explain the setup of the numerical simulations and the determination of the used simulation parameters for B4Q, C45 steel, and Al 7075 T6. Then, velocity time curves produced in numerical simulations and the Hugoniot results derived from these curves are compared with the corresponding experimental results. Based on this comparison of experimentally derived values with those stemming from a perfectly homogenous numerical concrete material model, the previously identified outliers in the data

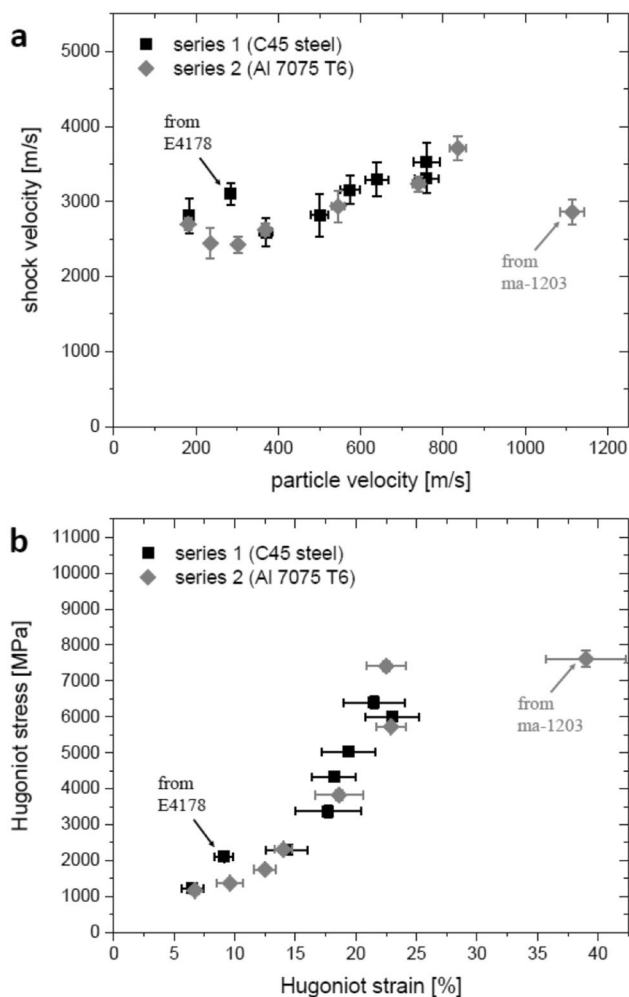


Fig. 3 Presentation of the obtained shock velocity over particle velocity data (a) together with the Hugoniot stress over strain data (b). All values and error bars are given in Table 1

are discussed. Finally, a study of the parameters describing the pressure dependence of the failure surface is conducted in order to investigate their influence on the simulated velocity time curves.

Setup of Numerical Simulations and Determination of Simulation Parameters

The setup of the numerical simulations of PPI consists of rows of two-dimensional cells to which rigid boundary conditions are applied that only allow motion in the direction of the impact velocity. Consequently, the square shaped cells (length of 0.01 mm) of the projectile (backing plate and specimen) and the target (witness plate) exhibit a perfectly one-dimensional strain state throughout the entire simulation. An illustration of this setup and a more detailed discussion is available in [34]. These applied simplifications are proper assumptions as long as edge effects and consequences

of fracture and spallation can be neglected. Due to the geometry of the thin plates and the setup of the inverse PPI experiment, a significant deviation from a one-dimensional strain state can be excluded for the regarded time interval of the free surface velocity time curves [34, 35]. All numerical simulations were performed with the thicknesses of the plates given in Fig. 1, using the commercial hydrocode [46] software ANSYS-AUTODYN [47], Version 19.1, analog to [34]. Corresponding to the VISAR measurement of the free surface velocity, the velocity in impact direction is recorded in the last cell of the witness plate as a function of time in the simulation. Both of these (numerical and experimental) velocity time curves can directly be compared to one another in order to discuss their agreement.

In the numerical simulations of PPI, the B4Q specimen material is described with the RHT model [4, 48]. For details on this model, we would like to refer the reader to the original [4, 48] and recently provided summaries of the model in [7, 49]. Most importantly for PPI, the RHT model employs a p - α -EOS [50] with a polynomial solid EOS of 3rd order that includes an energy dependence.

The parameter set used for the B4Q material in this work is presented in Table 2. From these parameters, the porous density, the uniaxial (unconfined), compressive strength, and the tensile strength have been directly measured. The tensile strength fraction (f_t/f_c) follows directly, while the shear strength fraction (f_s/f_c) is assumed to exhibit a similar ratio to the tensile strength fraction as in other concrete materials [3, 48]. In six Split Hopkinson Bar (SHB) tests, the mean value of the longitudinal velocity in a bar was measured as $c_1 = 4770$ m/s and assuming a Poisson's ratio of 0.20 [2], the shear modulus and the porous sound speed were calculated. From these SHB tests, a mean dynamic increase factor of the tensile strength of 2.6 at a mean strain rate of 56 1/s has been determined. Using the usual formula for the dynamic increase of tensile strength of the RHT-model [48, 49], the tensile strain rate exponent δ is derived. With this δ and the assumption of a relevant strain rate of 10^5 1/s, the principal tensile failure stress value is calculated with the same formula. Additionally, the compressive strain rate exponent α is calculated by the corresponding formula for the dynamic increase of compressive strength [48, 49] with the measured uniaxial, compressive strength value of $f_c = 140$ MPa. The latter value is furthermore used to obtain the initial compaction pressure by setting this value to 2/3 of f_c [48, 49]. All other strength and failure parameters in Table 2 are taken from a previously published parameter set for a UHPC in [3].

All of the just discussed parameters have been held constant during parameter studies of the remaining EOS parameters in PPI simulations with the experimentally determined impact velocities (Table 1). In these parameter studies, EOS parameters of other parameter sets of concrete [3, 48] were

Table 2 Material parameter set used for B4Q in AUTODYN implementation [47, 48]

B4Q 140 MPa			
<i>Equation of state</i>	<i>P alpha</i>	<i>Strength</i>	<i>RHT concrete</i>
<i>Reference density</i>	2.75 g/cm³	Shear modulus G	22.7 GPa
<i>Porous density</i>	2.39 g/cm³	Compressive strength (f_c)	140 MPa
<i>Porous sound speed</i>	3560 m/s	Tensile strength (f_t/f_c)	0.069
<i>Initial compaction pressure</i>	93.3 MPa	Shear strength (f_s/f_c)	0.12
<i>Solid compaction pressure</i>	6.0 GPa	Intact failure surface constant A	2.01
<i>Compaction exponent</i>	5	Intact failure surface exponent n	0.636
<i>Solid EOS</i>	<i>Polynomial</i>	Tens./comp. meridian ratio (Q)	0.6805
<i>Bulk modulus A1</i>	35.27 GPa	Brittle to ductile transition	0.0105
<i>Parameter A2</i>	60 GPa	G (elast.)/(elast. plast.)	2.31
<i>Parameter A3</i>	10 GPa	Elastic strength/ f_t	0.95
<i>Parameter B0 = Γ</i>	1.22	Elastic strength/ f_c	0.70
<i>Parameter B1 = Γ</i>	1.22	Fractured strength constant B	2.01
<i>Parameter T1 = A1</i>	35.27	Fractured strength exponent m	0.636
<i>Parameter T2</i>	0 kPa	Compressive strain rate exponent α	0.009
<i>Reference temperature</i>	300 K	Tensile strain rate exponent δ	0.057
<i>Specific heat</i>	654 J/kg K	Max. fracture strength ratio	1.0×10^{20}
<i>Thermal conductivity</i>	0 J/mK s	Use cap on elastic surface?	<i>Yes</i>
<i>Compaction curve</i>	<i>Standard</i>	<i>Failure</i>	<i>RHT concrete</i>
		Damage constant D1	0.04
Erosion	<i>None</i>	Damage constant D2	1.0
		Minimum strain to failure	0.01
		Residual shear modulus fraction	1.0
		Tensile failure	<i>Principal stress</i>
		Princ. tensile failure stress	39 MPa
Friction plate material/B4Q	0.1	Max. princ. stress difference/2	1.01×10^{20} kPa
		Crack softening	<i>Yes</i>
		Fracture energy, G_f	10 kJ/m ²
		Onset compression after failure	0
		Flow rule	<i>No bulking</i>
		Stochastic failure	<i>No</i>

For information on the RHT model in LS-DYNA implementation, see [7]. The EOS parameters of B4Q, dominant in the present work, are in bold italics

tested primarily. From these different starting points, EOS parameters were varied within a physically reasonable interval. Comparing the resulting velocity time curves of these simulations with the experimentally determined free surface velocity time curves, allowed us to assess the ability of the employed EOS parameters to reproduce the data. In Table 2, the EOS parameters which resulted in the most satisfying agreement between the simulated and the measured curves are given. Interestingly, from the EOS parameters obtained in the parameter study, only the compaction exponent and the solid EOS parameters A2 and A3 vary from the parameters of the conventional strength concrete in [48], while the rest are equal. This includes the key EOS parameters of the reference density, the solid compaction pressure, the bulk modulus ($A1 = T1$) and the Grüneisen parameter Γ ($= B0 = B1$). Apparently, the EOS of the B4Q material

investigated in the current work shares some key properties with the EOS of conventional concrete [27, 48].

The material models and the corresponding parameter sets used for the plate materials in the PPI simulations are given in Table 3. For C45 steel, all parameters are taken from [26], except the yield stress value. For this parameter, a value is chosen that reproduces the observed Hugoniot elastic limit of 36 m/s. For Al 7075 T6, all parameters are taken from [45].

Comparison of Velocity Time Curves

In Fig. 4, the measured free surface velocity time curves are compared with the corresponding curves from the PPI simulations employing the final parameter set for B4Q given in Table 2. In order to keep this presentation comprehensible,

Table 3 Material parameters for C45 steel (plate material series 1) and Al 7075 T6 (plate material series 2) in AUTODYN [47] implementation

C45 steel			
Reference density	7.8 g/cm ³	Strength	<i>von Mises</i>
Equation of state	<i>Shock</i>	Shear modulus	81 GPa
Grüneisen coefficient Γ	1.664	Yield stress	500 MPa
Parameter C1	4483 m/s		
Parameter S1	1.332	Failure	<i>None</i>
Reference temperature	300 K		
Specific heat	420 J/kg K	Erosion	<i>None</i>
Thermal conductivity	0 J/mK s		
Al 7075 T6			
Reference density	2.804 g/cm ³	Strength	<i>Steinberg Guinan</i>
Equation of state	<i>Shock</i>	Shear modulus	26.7 GPa
Grüneisen coefficient Γ	2.2	Yield stress	420 MPa
Parameter C1	5200 m/s	Maximum yield stress	810 MPa
Parameter S1	1.36	Hardening constant	965
Reference temperature	300 K	Hardening exponent	0.1
Specific heat	848 J/kg K	Derivative dG/dP	1.741
Thermal conductivity	0 J/mK s	Derivative dG/dT	− 16.45 MPa/K
Failure	<i>None</i>	Derivative dY/dP	0.02738
Erosion	<i>None</i>	Melting temperature	1220 K

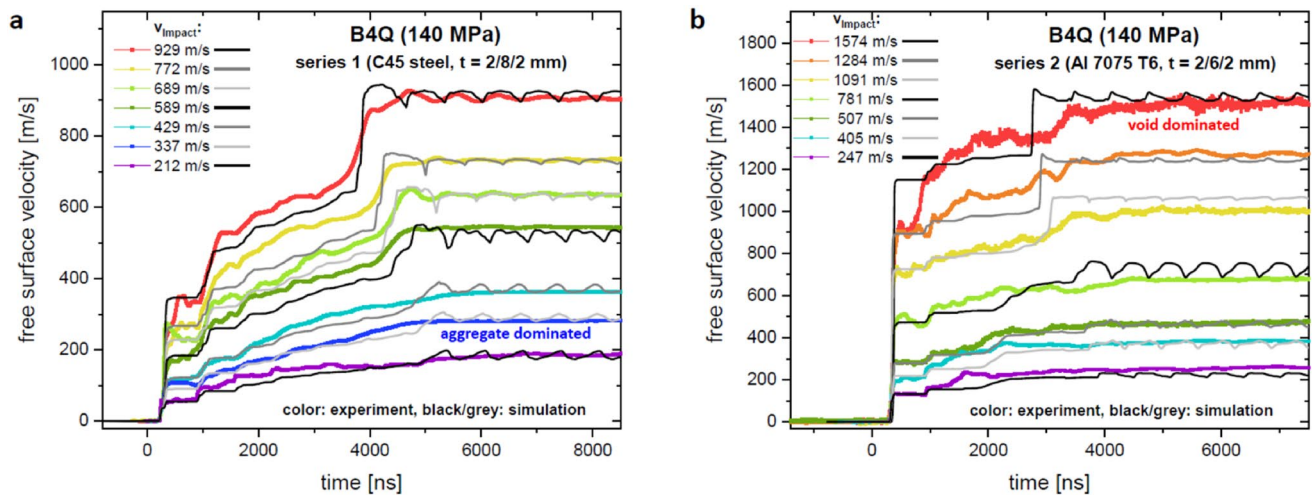


Fig. 4 Comparison of simulated and experimentally determined free surface velocity time curves for both conducted series of planar plate impact experiments with the ultra-high performance concrete B4Q.

the curves with $v_{imp} = 919$ m/s for (a) and the curves with $v_{imp} = 312$ m/s for (b) are omitted. From the comparison of these two pairs of curves, no additional conclusions can be drawn.

At first glance, the overall agreement between data and simulation results in Fig. 4 is good for both series. This general observation shows that the perfectly one-dimensional strain state realized in the simulation is also a sufficiently accurate assumption for these experimental setups. Especially a significant contribution of edge release effects can

be excluded on the basis of the overall agreement in Fig. 4. In particular, the final velocity of almost all simulated curves matches the one of the experimentally determined ones very well. The remaining deviation in the final velocities are small and can be explained by the experimental scattering of an inhomogeneous material. This agreement shows that the simulation adequately describes the conservation of energy during shock loading of B4Q.

Moreover, there is good agreement for the arrival times of the backing reflections and the heights of the first Hugoniot

plateaus in Fig. 4, with some exceptions and mostly moderate deviations. Mainly the two previously discussed experiments, corresponding to the dark blue curve ($v_{imp} = 337$ m/s) in (a) and the red one ($v_{imp} = 1574$ m/s) in (b), exhibit differences in the heights of the Hugoniot plateaus and in the arrival times of the backing reflections with respect to the simulated curves. At this point, the comparison with the curves of the perfectly homogenous numerical concrete model reveals that the deviations in these features are correlated for these experiments, which allows us to label them accordingly. Thus, the experiment E4178 ($v_{imp} = 337$ m/s) of series 1 is labeled “aggregate dominated”, since the higher Hugoniot plateau and the earlier arrival of the backing reflection point towards a dominating influence of the stiffer aggregates. The experiment ma-1203 ($v_{imp} = 1574$ m/s) of series 2, on the other hand, is labeled “void dominated”, because the lower Hugoniot plateau and the later arrival time of the backing reflection can be explained by a dominating contribution of an air void. In this context, the dark green curve with $v_{imp} = 589$ m/s should be discussed, since it shows that the mentioned features do not necessarily have to be correlated as obviously as in the cases of experiments E4178 ($v_{imp} = 337$ m/s) and ma-1203 ($v_{imp} = 1574$ m/s). Here, in comparison to the simulated curve, the earlier arrival of the backing reflection is not accompanied by a stable, higher Hugoniot plateau. However, the latter feature exhibits several small steps below and above the simulated plateau. Somewhat ambiguous features in the same experimental curve are thus occurring in this example, which might be explained by different magnitudes of influences by voids and aggregates at different times of the wave propagation in the sample. Beyond the two labeled curves, the otherwise proper reproduction of the heights of the Hugoniot plateaus by the simulations shows that the momentum conservation of B4Q under shock loading is adequately treated in the numerical model. Additionally, the mainly matching arrival times of the backing reflections in Fig. 4 suggest that the average wave propagation speed under shock and re-shock is also properly described by the PPI simulations with B4Q.

In contrast to the general agreement of the so far discussed features, for the heights of the release plateaus, there are obvious differences found between the simulated curves and the ones obtained from both experimental series. Nearly all the free surface velocity time curves from the experiments exhibit slightly but consistently higher release plateaus than the corresponding simulated curves in Fig. 4. Simultaneously, the timing of the release plateaus appears to match for almost all curves. During the parameter studies of the EOS parameters not determined experimentally, no combination of parameters could be found to reach an agreement between simulation and experiment for all features in the velocity time curves. Hence, the disagreement in the height of the release plateaus has been accepted to achieve

the otherwise proper reproduction of the other features in the experimentally obtained curves. The mismatch of this feature in Fig. 4 somewhat points to a phenomenological shortcoming of the employed EOS regarding shock release for which no explanation can be given at this point.

In conclusion, with the exception of the heights of the release plateaus, all observed features in the experimentally obtained free surface velocity time curves are adequately reproduced by the simulated curves in Fig. 4. Excluding two identified experimental outliers, the remaining small deviations are well within the expected experimental scattering of an inhomogeneous material like B4Q. We thus find that the used numerical model and in particular the employed EOS parameters are capable of a quantitatively correct description of the shock loading of B4Q.

Comparison of Hugoniot Results

An approach entirely equivalent to the one for the experimental curves is employed here to obtain Hugoniot results from the simulated PPI curves of the previous subsection. Thus, the heights of the first Hugoniot plateaus of the numerically obtained velocity time curves are used to calculate numerical Hugoniot results. Applying Eqs. (1)–(7) together with the constants previously given for C45 steel and Al 7075 T6, we obtain the values presented in Table 4. In addition to the experimentally realized impact velocities, smaller and larger impact velocities have also been chosen in PPI simulations to obtain additional values of Hugoniot plateaus and corresponding Hugoniot results. This numerical extrapolation of the Hugoniot results (labelled “ext” in Table 4) will be used in the following section for a comparison to other data beyond the range of the experiments conducted in this work.

In Fig. 5, the Hugoniot data given in Table 1 and presented in Fig. 3 is compared to the corresponding numerical results given in Table 4. The latter stems from a perfectly homogenous B4Q material model with shock properties that are successfully validated with several features (see Fig. 4 and discussion) of the experimentally obtained free surface velocity time curves and hence include experimental information beyond the height of the experimentally found Hugoniot plateaus. The fact that the experimental information from all curves is somehow considered in the validation of the simulation model makes the numerical Hugoniot results in Table 4 an average shock response of the investigated B4Q material. However, compared to a fit with an analytical function, using validated EOS parameters in a proper numerical model constitutes a more physics based approach towards an average of experimentally derived Hugoniot data.

The agreement between experimental and numerical Hugoniot results in Fig. 5 is good for all data points except the ones previously discussed and marked as “aggregate

Table 4 Values of Hugoniot plateaus $u_{s,2}$ resulting from simulations conducted with impact velocities v_{imp} and derived shock results (Hugoniot stress σ_H , strain ϵ , particle velocity u_p , and shock velocity U_s) for series 1 (C45 steel plates, thicknesses 2.0/8.0/2.0 mm) and series 2 (Al 7075-T6 plates, thicknesses 2.0/6.0/2.0 mm)

Simulation number	v_{imp} (m/s)	$u_{fs,2}$ (m/s)	σ_H (MPa)	ϵ_{B4Q} (%)	$u_{p,B4Q}$ (m/s)	$U_{s,B4Q}$ (m/s)
Series 1						
S1.ext1	50	14	318	1.4	43	3097
S1.ext2	150	39	895	4.5	131	2870
S1.1	212	55	1177	6.9	185	2670
S1.2	337	91	1817	11.2	292	2608
S1.3	429	122	2373	13.6	368	2698
S1.4	589	184	3501	16.9	497	2947
S1.5	689	228	4313	18.3	575	3138
S1.6	772	268	5060	19.2	638	3319
S1.7	919	341	6445	20.8	749	3603
S1.8	929	346	6541	20.9	756	3620
S1.ext3	1000	381	7216	21.7	810	3730
S1.ext4	1300	547	10,503	24.0	1027	4281
S1.ext5	1600	717	14,017	26.3	1242	4724
S1.ext6	1900	893	17,814	28.3	1454	5128
S1.ext7	2200	1075	21,909	30.2	1663	5514
S1.ext8	2500	1260	26,248	31.8	1870	5873
Series 2						
S2.ext1	50	31	274	1.0	35	3321
S2.ext2	100	57	503	2.4	72	2946
S2.ext3	200	109	963	5.3	146	2769
S2.1	247	133	1174	6.6	181	2723
S2.2	312	167	1465	8.5	229	2683
S2.3	405	218	1848	11.3	296	2612
S2.4	507	279	2312	14.0	368	2633
S2.5	781	473	3836	18.5	545	2948
S2.6	1091	726	5931	21.4	728	3409
S2.7	1284	893	7381	22.7	838	3688
S2.8	1574	1149	9707	24.6	1000	4063
S2.ext4	1800	1349	11,611	26.1	1126	4316
S2.ext5	2100	1623	14,343	27.7	1289	4657
S2.ext6	2400	1899	17,240	29.2	1451	4973
S2.ext7	2700	2180	20,338	30.5	1610	5285
S2.ext8	3000	2461	23,587	31.7	1770	5577
S2.ext9	3300	2747	27,049	32.8	1927	5875

Simulations for the numerical extrapolation are indicated by the “ext” in the simulation number

dominated” and “void dominated”. They correspond to the curves in Fig. 4, which are labeled accordingly and their deviation to the rest of the data is discussed in the previous subsection. The agreement in Fig. 5 is of course expected from the previously discussed match of the Hugoniot plateaus in Fig. 4 but the presentation in Fig. 5 clearly demonstrates how small the deviations are with respect to the shock velocity vs. particle velocity and the Hugoniot stress vs. strain values.

A very close investigation of the numerical results in Fig. 5 reveals a small difference between the data points of series 1 (red squares) and series 2 (blue diamonds), especially at larger particle velocities and strains. Since the data

points stem from the exact same numerical model of B4Q, this small difference likely originates from one of the numerical models for one of the plate materials or from the material constants of these materials employed in the calculation of the Hugoniot values. However, due to the fact that this small difference is clearly below the experimental accuracy of the experimentally derived Hugoniot data, it will not be considered here or in the following discussions.

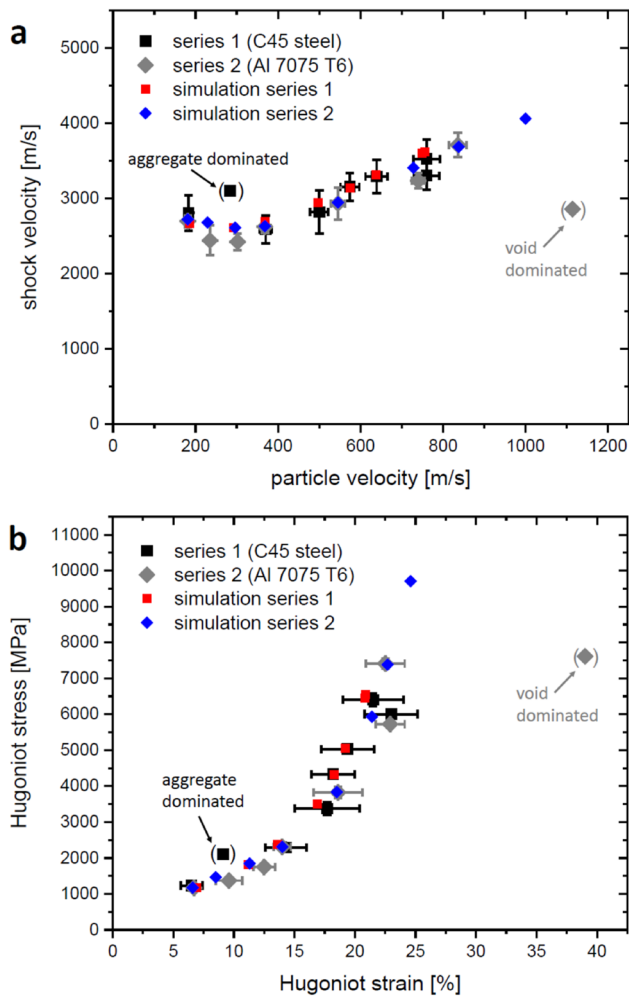


Fig. 5 Comparison of experimentally determined shock velocity over particle velocity data (**a**) and axial Hugoniot stress over Hugoniot strain data (**b**) with corresponding values derived from simulated curves. Values derived from experiments are given in Table 1 and those from simulations in Table 4 (Color figure online)

Influence of Failure Surface Parameters on Velocity Time Curves

Many strength parameters in the applied parameter set given in Table 2 are taken from a parameter set for UHPC in [3]. Especially the parameters of the pressure dependence of the ultimate strength (the so-called “failure surface”) of this parameter set [3] are not directly derived from triaxial tests but stem from a regression function based on data acquired for concretes with lower compressive strengths [2]. Moreover, the strength parameters taken from [3] are validated with impact experiments at impact velocities below 400 m/s with a rather soft projectile [38]. With the distinct pressure dependence of concrete strength, it is hence unclear if the employed strength modelling is appropriate for the very high stresses and strain rates occurring in inverse

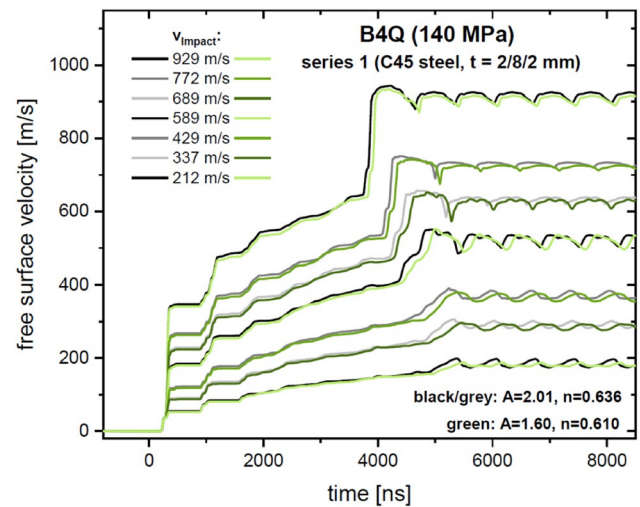


Fig. 6 Comparison of free surface velocity time curves obtained with the B4Q parameter set given in Table 2 (black/grey) and corresponding curves produced with varied failure surface parameters A and n (green) (Color figure online)

PPI. Consequently, the question about the influence of the employed failure surface on the simulated velocity time curves and the determined EOS parameters arises. In the case of a significant influence by an inappropriate treatment of the failure surface on the velocity time curves, the EOS parameters derived in parameter studies might be inappropriate as well. In this scenario, EOS parameters could be chosen so that the influence of the inappropriate strength treatment is compensated and a reproduction of the data is thus based on error cancelation. In order to exclude such a flawed determination of EOS parameters in our work, we test the influence of key strength parameters on the velocity time curves. For this parameter study, we vary the parameters of the pressure dependence of the failure surface [48, 49]. In the RHT model, the parameters of the intact failure surface (constant A and exponent n in Table 2) are varied together with the fractured strength parameters (constant B and exponent m in Table 2), so that $A=B$ and $n=m$. For this parameter study, we choose the values of a conventional strength concrete [48] in order to use physically reasonable parameters that, at the same time, constitute a significant change.

In Fig. 6, the results of the parameter variation from $A=B=2.01$ and $n=m=0.636$ (see Table 2) to $A=B=1.60$ and $n=m=0.610$ (from [48]) are displayed for the impact velocities and the setup of series 1. The velocity time curves produced with the parameter set of this work (black/grey) show small differences in all features compared to the corresponding curves using the parameter set with the altered values for A and n (green). The observed differences are clearly below the experimental scattering of the free surface velocity curves of B4Q (see Figs. 2 and 4) and would not

lead to a significant alteration of EOS parameters derived in a parameter study. Larger differences in strength parameters, however, might in fact lead to such an alteration of derived EOS parameters, since the performed parameter variation leads to visible differences in Fig. 6. At this point, it is not clear how much strength parameters validated for example with high velocity impact experiments would differ from the ones in this work (Table 2), so a definitive conclusion on the independence of our derived EOS parameters cannot be given. In any case, the significant alteration of strength parameters in this study suggests that the derived EOS parameters should not be significantly influenced by the employed strength modelling and hence should be appropriate for applications of shock loading of B4Q.

Numerical Extrapolation and Comparison to Literature Data

In this section, the Hugoniot data of this work is compared to partially reevaluated earlier work [27] and recently published results on concrete [29] and mortar [31, 33]. For more extensive comparisons, including several additional Hugoniot data sets, we would like to refer the reader to [27, 33]. On the one hand, the aim of the following comparison is to relate the current results to our earlier work [27] on mortar and meso-mechanical simulations of normal and high-strength concretes. On the other hand, a comparison to recent work on mortar [31, 33] is chosen, since these materials are also in the high-strength regime. The selected work on concrete [29] consists of a large data set on many different concrete formulations, which allows a comparison to a representative mean shock response of concrete varieties. Beyond these selected works, we prefer to omit the inclusion

Table 5 Reevaluation and reprint of the data of [27, 51]. Experimentally determined impact velocities v_{imp} and Hugoniot plateaus $u_{fs,2}$ together with derived shock material data (Hugoniot stress σ_H , strain ϵ , particle velocity u_p , and shock velocity U_s) for conventional and high-strength mortar. Data from shock reverberation analysis is reprinted from [27] and indicated by “rvb”

Experiment number	v_{imp} (m/s)	$u_{fs,2}$ (m/s)	σ_H (MPa)	ϵ_{B4Q} (%)	$u_{p,B4Q}$ (m/s)	$U_{s,B4Q}$ (m/s)
Conventional mortar						
ZeSII193	519	89	2003	22.7	475	2090
ZeSII194	493	84	1914	21.5	451	2101
ZeSII196	1018	280	5488	28.4	878	3094
ZeSII197	948	275	5395	24.6	811	3295
ZeSII198	742	150	3096	29.0	667	2297
ZeSII199	712	142	2951	28.1	641	2279
ZeSII200	960	248	4891	28.9	836	2896
ZeSII202	303	83	1897	7.3	262	3590
ZeSII203	305	50	1137	13.9	280	2010
ZeSII205	192	32	728	8.6	176	2047
ZeSII242rvb	928	–	4330	30.1	803	2670
ZeSII242rvb	928	–	10,600	33.0	1320	3990
ZeSII243rvb	808	–	3540	28.3	705	2480
ZeSII243rvb	808	–	8550	32.6	1170	3600
ZeSII244rvb	936	–	4380	30.2	810	2680
ZeSII244rvb	936	–	10,300	35.5	1340	3780
High-strength mortar						
Con2498	473	118	2520	15.2	414	2730
Con2499	495	117	2502	17.0	437	2570
Con2500	1050	362	7043	23.9	869	3634
Con2503	838	251	4947	22.9	713	3113
Con2505	1011	375	7292	20.7	824	3971
Con2506	249	62	1410	7.5	218	2900
Con2501rvb	978	–	13,500	31	1370	4419
Con2501rvb	978	–	18,030	34	1663	4861
Con2502rvb	480	–	5090	21	697	3274
Con2502rvb	480	–	6600	24	849	3484
Con2504rvb	829	–	10,000	29	1136	3948
Con2504rvb	829	–	13,700	31	1381	4448

of further data from literature in order to keep the data presentation reasonably comprehensible. For the comparison of our current experimental and simulated results to other data sets, we present all values in Table 1 and Table 4. Moreover, the partially reevaluated Hugoniot data from [27, 51] is given in Table 5 together with some reprinted data. This complete presentation of our current and previous Hugoniot data enables the reader to perform any desired comparison.

To allow a consistent comparison of the data of earlier work [27, 51] with the data in this work, a partial reevaluation of the data in [27, 51] is performed. In contrast to this work and other more recent publications [30, 32, 34], the calculation of the Hugoniot data in [27] does not take the contribution of the Hugoniot elastic limit of the plate material into account. While this is a reasonable assumption for shock states far above this Hugoniot elastic limit, there is a significant contribution in its vicinity. We consequently use the heights of the Hugoniot plateaus and the impact velocities given in [27, 51] together with Eqs. (1)–(7) to obtain the reevaluated data in Table 5. These calculations employ all above given constants for C45 steel with the exception of the value of the Hugoniot elastic limit, that is $u_{HEL,steel} = 75$ m/s for the hardened C45 steel in [27], as in other earlier work [30, 32, 34, 35]. Additionally, the densities of conventional ($f_c = 35$ MPa) mortar of 2.02 g/cm³ and high-strength ($f_c = 135$ MPa) mortar of 2.23 g/cm³ are used [27]. For the sake of completeness, the Hugoniot data derived from shock reverberation PPI tests in [27] is reprinted in Table 5 and indicated by “rvb”. Since this data stems from differences of velocity plateau heights in the free surface velocity time curves, it is unaffected by the change in the calculation formulas.

The Hugoniot data of the current work roughly lies within intervals of particle velocities from 180 to 840 m/s and stresses from 1.1 to 7.5 GPa (see Table 1, outliers not considered). Hence, a direct comparison to other data is technically restricted to this regime. However, by producing a validated numerical model for B4Q in this regime, we can use this numerical description to extrapolate the numerical Hugoniot results beyond the measured range. This numerical extrapolation of the shock response of B4Q is based on the p – α EOS [50], a polynomial solid EOS of 3rd order with energy dependence [48, 49], and a parameter set that is successfully validated with several experimental features in the free surface velocity time curves of two experimental series. Furthermore, we expect that none of the aggregate materials undergoes a phase change within the stress regime reached in these simulations. Hence, this physics based and validated extrapolation should be a reasonably accurate approximation for a comparison to literature data outside of the range of the Hugoniot data from Table 1. Consequently, the entire numerical Hugoniot results given in Table 4 (regular and

extrapolated) are used for the following comparison with literature data.

In Fig. 7a, our entire Hugoniot results on concrete and mortar are presented as shock velocities U_s over particle velocities u_p in a particle velocity range that is chosen to include all values of the experimental data (series 1 and series 2 of this work; “Riedel mortar conv.” and “Riedel mortar high” from [27, 51], partial reevaluation and reprint in Table 5). Furthermore, the numerical Hugoniot results (regular and extrapolated of this work) as well as the results of meso-mechanical simulations on conventional and high-strength concrete (“Riedel concrete conv.” and “Riedel concrete high” from [27]) are displayed. The latter simulations consist of numerical models that are validated with the corresponding mortar data and additionally use numerical models for aggregates that include parameters from literature [27]. Hence, the data on mortar and the results of the meso-mechanical simulations in Fig. 7a) are not independent but the simulated results for the conventional/high-strength concrete are partially based on the data of the conventional/high-strength mortar.

From our data in Fig. 7a, we can observe that in the regarded interval of particle velocities, there is a significant influence of strength properties on the Hugoniot data of mortar. The differences observed between B4Q and conventional mortar might stem from differences in strength or from influences of the aggregates (maximum grain size 8.0 mm) and steel fibers (1.0 vol%) in B4Q. However, the agreement of the B4Q data with the data on high-strength mortar at lower particle velocities suggests that influences of aggregates and steel fibers are quite small, since both materials should exhibit a similar strength. Then, in the region of higher particle velocities, a difference is observed between the Hugoniot data of high-strength mortar and the numerically extrapolated values of B4Q. Lastly, the meso-mechanical simulation of the two concretes defines a band in which the new data and simulation results of B4Q are situated. As a guide to the eye, the values of the meso-mechanical simulations are thus displayed with connecting lines. Within this band, it appears that at lower particle velocities, the shock response of B4Q is close to the one of conventional concrete, while it approaches more and more the one of high-strength concrete for higher u_p values. In conclusion, our Hugoniot data in Fig. 7a) suggests that material strength as well as the admixture of aggregates (and steel fibers) influence the shock response of mortar/concrete, with strength effects appearing to be more important. The corresponding presentation of this data as Hugoniot stress over strain in Fig. 7b) supports these findings and does not allow any additional conclusions.

In Fig. 7b), recently published Hugoniot data from Erzar et al. [31] for a high-strength mortar is shown as well, since

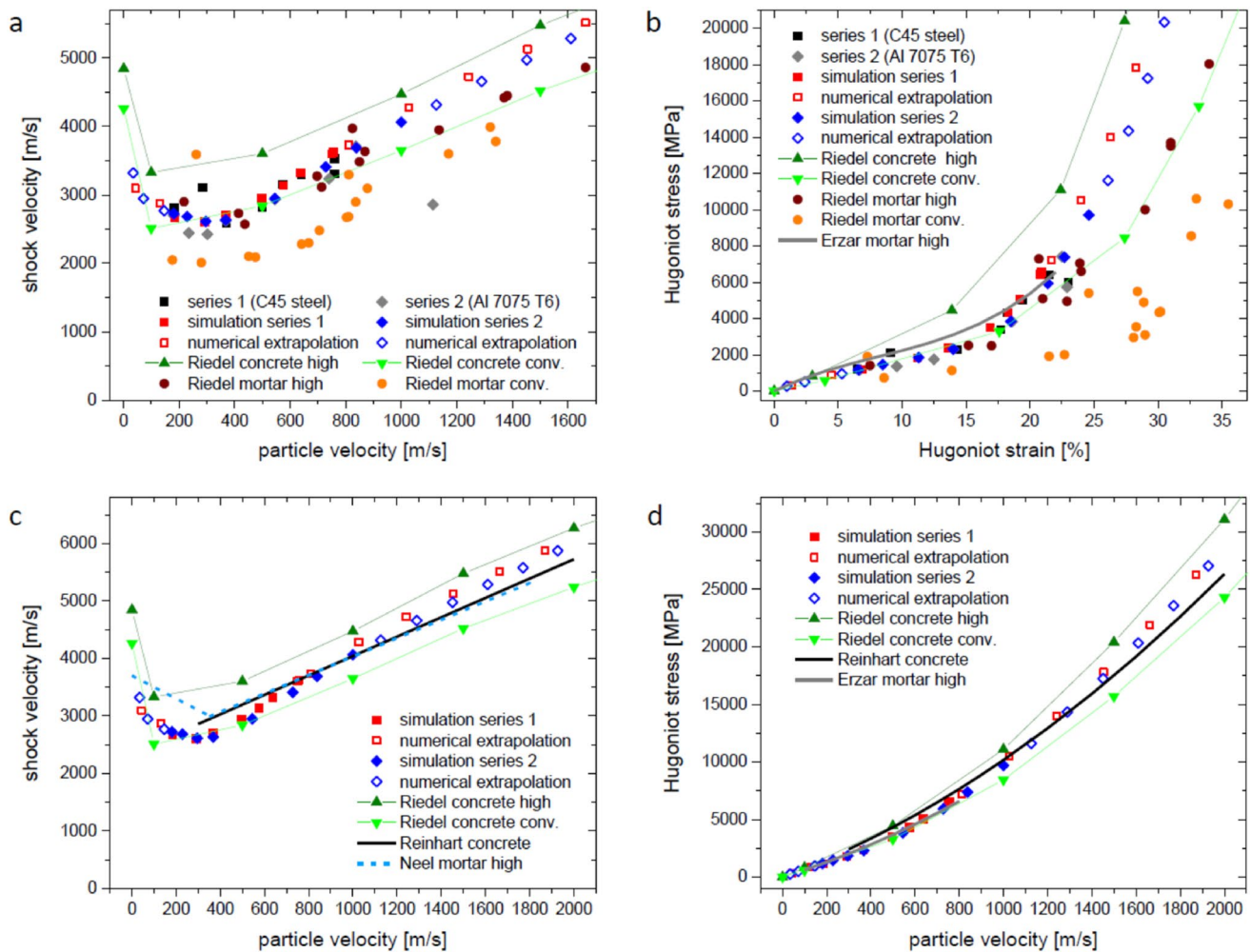


Fig. 7 Comparison of the Hugoniot results of this work with previous, partially reevaluated own work [27, 51] (a, b) and recently published results on concrete [29] and mortar [31, 33] (b–d) (Color figure online)

this data is given in terms of Hugoniot stress over strain (and over particle velocity). For stresses up to 6 GPa, the data is available in [31] in the form of fit functions and is thus displayed as such (grey curve) in comparison to our own results. The data of Erzar et al. [31] is quite similar to the data of this work and the high-strength mortar of Riedel et al. [27], since only a small tendency towards higher stresses can be observed in the regime of smaller strains. This agreement corroborates the finding from Fig. 7a that mortar and concrete of similar strength properties exhibit a similar shock response below stresses of roughly 6 GPa.

The Hugoniot data of Reinhart [29] on several different concrete materials spans over a strength regime from 35 to almost 200 MPa and provides shock velocities for a particle velocity range of roughly 300 to 2000 m/s. The values for conventional and high-strength concretes with and without aggregates and/or steel fibers are fitted with a single linear relation, which is displayed as a black line in Fig. 7c. Here,

its comparison in the range of the data from Reinhart [29] with the numerical Hugoniot results of our work and the meso-mechanical results from Riedel et al. [27] is shown. The omission of the experimental data given in Fig. 7a and the choice of the linear fit rather than the data values from Reinhart [29] are meant to increase the comprehensibility of this comparison. Accordingly, the very recently published bilinear shock velocity over particle velocity relation of Neel [33] is displayed as blue dashed lines in Fig. 7c. This bilinear fit corresponds to a high-strength mortar (referred to as concrete in [33] for historical reasons) and originates from data produced in PPI tests with a variety of different configurations. The range of experimentally realized particle velocities of this data goes up to almost 1800 m/s. In Fig. 7c, the band defined by the results of the meso-mechanical simulations of the two concretes of Riedel et al. [27] includes both fits of Reinhart [29] and Neel [33], with the latter two being almost identical to each other above

$u_p = 350$ m/s. In addition, all four of these data sets exhibit a very similar slope above $u_p = 500$ m/s. Compared to the results of Neel [33], the here derived Hugoniot data of B4Q exhibits a somewhat smaller minimum of U_s that is situated at a slightly lower u_p value. From there, the values of B4Q increase a little steeper than the two linear fits of Reinhart [29] and Neel [33] and end up at slightly higher U_s values above $u_p = 1300$ m/s.

Despite the observed differences in Fig. 7c, the values displayed there can be regarded as reasonably consistent, especially considering the inhomogeneous nature of concrete materials. The plot in Fig. 7d, which presents the available results as Hugoniot stress over particle velocities agrees with this finding. So overall, it is only the data of conventional mortar (Table 5) of Riedel et al. [27] which significantly deviates from the general trend in Fig. 7 and lies clearly below the other displayed results. All other discussed deviations in Fig. 7 can be considered rather small and are regarded as somehow minor, material specific characteristics within a larger, consistent picture of the shock response of concrete and mortar materials. Interestingly, the results of the meso-mechanical simulations of conventional and high-strength concrete of Riedel et al. [27] can be interpreted as the frame of this picture.

Conclusion

In this work, we present inverse planar plate impact (PPI) experiments with the ultra-high performance concrete B4Q together with corresponding numerical simulations. By successfully reproducing the experimental free surface velocity time curves with these numerical simulations, we obtain a validated numerical model for B4Q. In the comparison of the simulated and the experimentally obtained curves, the Hugoniot plateaus, the arrival times of the backing reflections, and the reached final velocities are in reasonably good agreement for an inhomogeneous material like B4Q. At the same time, the height of the release plateaus in the experimental curves is generally less well reproduced. However, considering the overall agreement between experiment and simulation, we present validated equation of state (EOS) model parameters that should lead to reasonably accurate hydrocode predictions in applications to shock loading scenarios of B4Q.

The free surface velocity time curves obtained in the two conducted experimental PPI series with two different witness plate materials are used to derive Hugoniot data of B4Q in the range of particle velocities from 180 to 840 m/s and stresses from 1.1 to 7.5 GPa. Furthermore, we derive averaged numerical Hugoniot results from the simulations with the setups of both experimental series and compare them to the corresponding experimental data. The fact that

the Hugoniot data derived from two different experimental series and the corresponding numerical results turn out to be one consistent set of values renders them highly trustworthy. Any significant inconsistency stemming from one of the different plate materials or experimental issues should become visible in this comparison. Since the EOS parameters of B4Q are validated with experimental features beyond the first Hugoniot plateau from which the shock states are derived, the experimental and simulated values are at least partially independent of one another. Hence, including numerical Hugoniot results in this comparison provides additional consistency as well as a homogenized mean shock response of B4Q. In the same spirit, the comparison of experimental and simulated results, including the correlation of different features in the velocity time curves, allows us to clearly identify experimental outliers. Considering the comparatively small number of tests usually performed for experimental PPI series, single experimental outliers can significantly influence a derived mean shock response of an inhomogeneous material and possibly alter it towards an unrepresentative result. The probability for such errors is significantly reduced by our combined approach of experiments and simulations.

In order to investigate the influence of strength modelling on the velocity time curves, a parameter study of the pressure dependence of the failure surface in the applied RHT model is performed. The observed differences between the curves produced with a parameter set employing parameters from conventional concrete and the ones resulting from the otherwise used parameter set are visible but very small. Thus, we conclude that a significant influence of strength modelling on the derivation of EOS parameters should not be present for the used parameter set of B4Q. For a much larger difference in failure surface parameters than the one chosen in our parameter study, however, such an influence might become significant. Only a strength model that is validated in the appropriate pressure regime will be able to eventually resolve this issue.

In addition to the homogenization of experimental Hugoniot data and its applicability to shock loading scenarios, our derived numerical model can be used to extrapolate the simulated shock results. We demonstrate this physics based approach by simulating additional PPI tests with smaller and larger impact velocities and deriving numerical Hugoniot results beyond the experimentally realized stress and particle velocity range. Similarly, readers can use our numerical model and alter it with respect to their investigated concrete or mortar material or experimental setup to produce numerical Hugoniot results for any desired comparison or prediction. In addition, our model opens up the possibility for all sorts of sensitivity studies that can help clarifying certain influences of material parameters on the shock response of a concrete or mortar material. In this work, we

use the numerical extrapolation of the simulated Hugoniot results to enable a comparison to our own previously published results and selected literature data in the entire available stress and particle velocity range. In this comparison, we observe a consistent picture of the shock response of concrete and high-strength mortar materials, in which the discussed deviations can be considered somehow minor, material specific characteristics.

In this work, we provide a validated, full parameter set for applications of impact and blast loading of an ultra-high performance concrete. Furthermore, all derived experimental and numerical Hugoniot results of B4Q and the partially reevaluated Hugoniot data sets of conventional and high-strength mortar from earlier work are presented. We highly encourage readers to apply and use these results in order to further the ongoing discussion of the shock response of concrete and mortar materials.

Acknowledgements We thank the involved technicians at EMI for the production of B4Q, the preparation of samples, and performing the planar plate impact experiments. Furthermore, we would like to thank Dr. H. Sohn for his kind support.

Funding Open Access funding enabled and organized by Projekt DEAL. We acknowledge funding by the Federal Office of Bundeswehr Equipment, Information Technology and In-Service Support (BAAw) and the Federal Ministry of Defence (BMVg).

Code availability Simulations are performed with the commercial hydrocode software ANSYS-AUTODYN (Version 19.1).

Declarations

Conflict of interest The authors declared that they have no conflict of interest.

Open Access This article is licensed under a Creative Commons Attribution 4.0 International License, which permits use, sharing, adaptation, distribution and reproduction in any medium or format, as long as you give appropriate credit to the original author(s) and the source, provide a link to the Creative Commons licence, and indicate if changes were made. The images or other third party material in this article are included in the article's Creative Commons licence, unless indicated otherwise in a credit line to the material. If material is not included in the article's Creative Commons licence and your intended use is not permitted by statutory regulation or exceeds the permitted use, you will need to obtain permission directly from the copyright holder. To view a copy of this licence, visit <http://creativecommons.org/licenses/by/4.0/>.

References

- Xue J, Briseghella B, Huang F, Nuti C, Tabatabai H, Chen B (2020) Review of ultra-high performance concrete and its application in bridge engineering. *Constr Build Mater* 260:119844
- Nöldgen M (2011) Modeling of Ultra High Performance Concrete (UHPC) under impact loading—design of a high rise building core against aircraft impact, *Forschungsergebnisse aus der Kurzzeitdynamik*. Fraunhofer Verlag, Heft 19
- Riedel W, Stolz A, Roller C, Nöldgen M, Laubach A, Pattberg G (2011) Impact resistant superstructure for power plants part i: box girders and concrete qualities, *transactions, SMiRT 21*, 6–11 November, 2011, New Delhi, India
- Riedel W (2009) 10 Years RHT: a review of concrete modelling and hydrocode applications. In: Hiermaier S (ed) *Predictive modeling of dynamic processes—a tribute to professor Klaus Thoma*. Springer, Cham
- Ellis BD, DiPaolo BP, McDowell DL, Zhou M (2014) Experimental investigation and multiscale modeling of ultra-high performance concrete panels subject to blast loading. *Int J Impact Eng* 69:95–103
- Li J, Wu C, Hao H (2015) Investigation of ultra-high performance concrete slab and normal strength concrete slab under contact explosion. *Eng Struct* 102:395–408
- Grunwald C, Schaufelberger B, Stolz A, Riedel W, Borrvall T (2017) A general concrete model in hydrocodes: verification and validation of the Riedel–Hiermaier–Thoma model in LS-DYNA. *Int J Prot Struct* 8(1):58–85
- Su Q, Wu H, Sun HS, Fang Q (2021) Experimental and numerical studies on dynamic behavior of reinforced UHPC panel under medium-range explosions. *Int J Impact Eng* 148:103761
- Dawson A, Bless S, Levinson S, Pedersen B, Satapathy S (2008) Hypervelocity penetration of concrete. *Int J Impact Eng* 35:1484–1489
- Liu J, Wu C, Su Y, Li J, Shao R, Chen G, Liu Z (2018) Experimental and numerical studies of ultra-high performance concrete targets against high-velocity projectile impacts. *Eng Struct* 173:166–179
- Chocron S, Walker JD, Grosch DJ, Beissel SR, Durda DD, Housen KR (2019) Hypervelocity impact on concrete and sandstone: momentum enhancement from tests and hydrocode simulations. In: *Proceedings of the 2019 hypervelocity impact symposium, HVIS2019-059*, 14–19 April 2019, Destin, FL
- Wu H, Hu F, Fang Q (2019) A comparative study for the impact performance of shaped charge JET on UHPC targets. *Defence Technol* 15:506–518
- Meyers MA (1994) *Dynamic behavior of materials*. Wiley, New York
- Hiermaier S (ed) (2009) *Predictive modeling of dynamic processes—a tribute to Professor Klaus Thoma*. Springer, Cham
- Gebbeken N, Greulich S, Pietzsch A (2006) Hugoniot properties of concrete determined by full-scale detonation experiments and flyer-plate-impact tests. *Int J Impact Eng* 32:2017–2031
- Tu H, Fung TC, Tan KH, Riedel W (2019) An analytical model to predict the compressive damage of concrete plates under contact detonation. *Int J Impact Eng* 134:103344
- Zukas JA (1990) *High velocity impact dynamics*. Wiley, New York
- Atou T, Sano Y, Katayama M, Hayashi S (2013) Damage evaluation of reinforced concrete columns by hypervelocity impact. *Procedia Eng* 58:348–354
- Murphy MJ, Kuklo RM (1999) Fundamentals of shaped charge penetration in concrete. In: *Proceedings of the 18th international symposium on ballistics*, San Antonio, TX, USA
- Marsh SP (ed) (1980) *LASL Shock Hugoniot Data*. University of California Press Ltd., London
- Trunin RF et al (2001) Experimental data on shock compression and adiabatic expansion of condensed matter. *Sarov: RFNC-VNIIEF*
- Grady D (1995) Shock equation of state properties of concrete, SAND95-2215C. Sandia National Laboratory, Albuquerque, NM
- Kipp ME, Chhabildas L, Reinhart W (1997) Elastic shock response and spall strength of concrete, SAND97-0464C. Sandia National Laboratory, Albuquerque, NM

24. Hall C, Chhabildas L, Reinhart W (1999) Shock Hugoniot and release in concrete with different aggregate sizes from 3 to 23 GPa. *Int J Impact Eng* 23:341–351
25. Reinhart W, Chhabildas L, Kipp ME, Wilson L (1999) Spall strength measurements of concrete for varying aggregate sizes. In: *Proceedings of the 15th US army symposium on solid mechanics*, Myrtle Beach, SC
26. Rohr I, Nahme H, Thoma K (2005) Material characterization and constitutive modelling of ductile high strength steel for a wide range of strain rates. *Int J Impact Eng* 31:401–433
27. Riedel W, Wicklein M, Thoma K (2008) Shock properties of conventional and high strength concrete: experimental und mesomechanical analysis. *Int J Impact Eng* 35:155–171
28. Rohr I, Nahme H, Thoma K, Anderson CE (2008) Material characterisation and constitutive modelling of a tungsten-sintered alloy for a wide range of strain rates. *Int J Impact Eng* 35:811–819
29. Reinhart WD (2012) Dynamic response of masonry materials. In: *Proceedings of the 12th hypervelocity impact symposium*, Baltimore, MD, USA
30. Lässig T, Nguyen L, May M, Riedel W, Heisserer U, van der Werff H, Hiermaier S (2015) A non-linear orthotropic hydrocode model for ultra-high molecular weight polyethylene in impact simulations. *Int J Impact Eng* 75:110–122
31. Erzar B, Pontiroli C, Buzaud E (2016) Shock characterization of an ultra-high strength concrete. *Eur Phys J Spec Top* 225:355–361
32. Hoerth T, Bagusat F, Hiermaier S (2017) Hugoniot data of Seeger sandstone up to 7 GPa. *Int J Impact Eng* 99:122–130
33. Neel C (2018) Compaction and spall of UHPC concrete under shock conditions. *J Dyn Behav Mater* 4:505–528
34. Sauer C, Bagusat F, Heine A, Riedel W (2018) Shock response of lightweight adobe masonry. *J Dyn Behav Mater* 4:231–243
35. Sauer C, Heine A, Bagusat F, Riedel W (2020) Ballistic impact on fired clay masonry bricks. *Int J Prot Struct* 11(3):304–318
36. Bauer S, Bagusat F, Strassburger E et al (2021) New insights into the failure front phenomenon and the equation of state of soda-lime glass under planar plate impact. *J Dyn Behav Mater* 7:81–106
37. Fehling E, Schmidt M, Teichmann T, Bunje K, Bornemann R, Middendorf B (2005) Entwicklung, Dauerhaftigkeit und Berechnung Ultra-Hochfester Betone (UHPC), *Schriftreihe Baustoffe und Massivbau*, Heft 1. University of Kassel, Kassel
38. Riedel W, Nöldgen M, Straßburger E, Thoma K, Fehling E (2010) Local damage to ultra high performance concrete structures caused by an impact of aircraft engine missiles. *Nucl Eng Des* 240(10):2633–2642
39. McMahon MI, Nelmes RJ (2006) High-pressure structures and phase transformations in elemental metals. *Chem Soc Rev* 35:943–963
40. Barker LM (1975) α -phase Hugoniot of iron. *J Appl Phys* 46(6):2544–2547
41. Barker LM, Hollenbach RE (1972) Laser interferometer for measuring high velocities of any reflecting surface. *J Appl Phys* 43:4669–4675
42. Barker LM, Schuler KW (1974) Correction to the velocity-perfringe relationship for the VISAR interferometer. *J Appl Phys* 45:3692–3693
43. Hemsing WF (1979) Velocity sensing interferometer (VISAR) modification. *Rev Sci Instrum* 50:73–78
44. Barker LM (1998) The accuracy of VISAR instrumentation. *AIP Conf Proc* 429:833–836
45. Steinberg DJ (1996) Equation of state and strength properties of selected materials. Report UCRL-MA-106439 (Change 1). Lawrence Livermore National Laboratory, Livermore
46. Zukas JA (2004) *Introduction to hydrocodes*, 1st edn. Elsevier, Amsterdam
47. AUTODYN Theory Manual (2005) Revision 4.3. Century Dynamics Ltd., Horsham
48. Riedel W, Kawai N, Kondo K (2009) Numerical assessment for impact strength measurements in concrete materials. *Int J Impact Eng* 36:283–293
49. Sauer C, Heine A, Riedel W (2017) Developing a validated hydrocode model for adobe under impact loading. *Int J Impact Eng* 104:164–176
50. Herrmann W (1969) Constitutive equation for the dynamic compaction of ductile porous materials. *J Appl Phys* 40:2490–2499
51. Riedel W (2004) Beton unter dynamischen Lasten – Meso- und makromechanische Modelle. In: Thoma K, Hiermaier S (eds) *Fraunhofer-Institut für Kurzzeitdynamik, Ernst-Mach-Institut EMI*, Freiburg i. Br., Fraunhofer-Verlag

Publisher's Note Springer Nature remains neutral with regard to jurisdictional claims in published maps and institutional affiliations.